# ChemComm



## COMMUNICATION

View Article Online



Cite this: Chem. Commun., 2025. **61**, 1854

Received 31st October 2024, Accepted 23rd December 2024

DOI: 10.1039/d4cc05786d

rsc.li/chemcomm



Haoyu Yin,<sup>a</sup> Jingfu Chen,<sup>a</sup> Junhong Tan,<sup>a</sup> Cheng Zhong,\*<sup>b</sup> Fei Wu\*<sup>a</sup> and Linna Zhu<sup>b</sup>\*

In this study, new carboxylates are synthesized for sodium-ion batteries. The bithiophene-based anode material BT demonstrates a high reversible capacity of 201 mA h g<sup>-1</sup> and excellent durability. BT retains 99.1% capacity after 400 cycles at 0.2C and 90.1% capacity after 1500 cycles at 2C, showing superior conductivity and stability.

Among the rechargeable batteries, sodium-ion batteries (SIBs) have attracted significant attention due to the abundance of sodium resources, low cost, and the similar physical and chemical properties of Na ions and Li ions. 1-6 Organic electrode materials (OEMs) composed of light elements such as C, H, O, N, and S are considered to have great application prospects in sodium-ion batteries due to their high sustainability, structural diversity, and flexible structural tunability.7-16 Among various organic anode materials, carboxylate compounds exhibit characteristics such as low redox potential (<1.0 V), high specific capacity, and long cycling life, and have aroused wide interest. 17-24 Moreover, the electrochemical performance of carboxylate compounds can be achieved through the modification of their molecular structures. 25-27

Although organic carboxylates show great promise as anode materials, they tend to have low electronic conductivity and are prone to dissolving in the electrolyte, leading to low utilization of active materials and rapid capacity loss during cycling. To address these challenges, it is necessary to improve the material conductivity and reduce solubility through rational structural design at the molecular level. Huang et al. reported sodium 2,2'-bipyridine-5,5'-dicarboxylate as an anode material for SIBs. By introducing pyridine groups to regulate the planarity of the molecules, the solubility of the material in the electrolyte was improved.<sup>28</sup> Wang et al. designed sodium 4,4-stilbene carboxylate with an extended

conjugation structure, which can enhance the electrochemical

In this paper, two sodium carboxylates with thiophene aromatic rings were constructed: sodium [2,2'-bithiophene]-5,5'-dicarboxylate (BT) and sodium 5-(4-carboxyphenyl) thiophene-2-carboxylate (PT). BT features a bithiophene core structure, while PT is based on a phenylthiophene core structure. In addition, the compound sodium [1,1'-biphenyl]-4,4'dicarboxylate (BP), which has been reported before, was also studied for comparison. Compared with phenylthiophene, bithiophene exhibits better planarity and improved  $\pi$ -conjugation, which are beneficial for enhancing molecular solubility and conductivity. BT demonstrates superior cycling and rate performance in sodium-ion half-cells compared with PT and BP. Specifically, at a current density of 0.2C, BT provides a high reversible capacity of 201 mA h g<sup>-1</sup> and retains 99.1% of its capacity after 400 cycles. We also compared the electrochemical performance of BT with other reported carboxylate organic anodes, with results shown in Table S1 (ESI†), indicating that BT possesses excellent electrochemical performance. In addition, during long-term cycling, the BT electrode exhibits a capacity retention of up to 90.1% even after 1500 cycles at 2C. Finally, we successfully assembled a full cell using BT as the anode and commercial sodium vanadate phosphate (NVP) as the cathode material. The full cell exhibited a reversible capacity of 82 mA h g<sup>-1</sup> and an 88% capacity retention after 200 cycles at a current density of 100 mA g<sup>-1</sup>, demonstrating the potential application of BT in sustainable sodium-ion batteries.

We first synthesized 5-(4-formylphenyl) thiophene-2-carbaldehyde (PTDA) through a simple Suzuki coupling reaction between 5-bromo-thiophene-2-carbaldehyde and (4-formylphenyl) boronic acid. Subsequently, PTDA underwent an oxidation reaction to obtain 5-(4-carboxyphenyl) thiophene-2-carboxylic acid (PTDC). Finally, PTDC undergoes a simple alkalization reaction to obtain PT. While BT is directly obtained through a one-step reaction from

performance.7 Meanwhile, studies have shown that conjugated structures containing heteroatoms (N, S, and O) typically exhibit good redox activity, making them suitable as electrode materials for rechargeable batteries.29

<sup>&</sup>lt;sup>a</sup> Chongqing Key Laboratory of Battery Materials and Technologies, School of Materials & Energy, Southwest University, Chongqing 400715, P. R. China. E-mail: feiwu610@swu.edu.cn, lnzhu@swu.edu.cn

<sup>&</sup>lt;sup>b</sup> Hubei Key Lab on Organic and Polymeric Optoelectronic Materials, Department of Chemistry and Molecular Science, Wuhan University, Wuhan 430072, P. R. China † Electronic supplementary information (ESI) available. See DOI: https://doi.org/

(a) Nac 1600 1400 1200 1000 ВР (d) 120 (c) 495 548 626 60

Communication

Fig. 1 (a) Molecular structures of BP, PT and BT; (b) FTIR spectra of BTDC and BT; (c) XRD of BT, PT and BP; and (d) thermogravimetric analysis of BT, PT and BP.

2,2'-bithiophene-5,5'-dicarboxylic acid (BTDC), BP is synthesized according to methods reported in the literature.<sup>30</sup> Note that BT could be obtained in a total yield of over 80%, and the final product PT also reaches a total yield of 66%. The structures of all newly synthesized compounds were confirmed by <sup>1</sup>H and <sup>13</sup>C nuclear magnetic resonance (NMR) spectroscopy.

The FTIR spectra of the intermediates BTDC and PTDC, as well as the final products BT and PT, are shown in Fig. 1b and Fig. S10 (ESI†). The spectra of BTDC and PTDC display the C=O stretching vibrations and O-H bending vibrations of the carboxylic acid (-COOH) group, at around 1653, 1310, and 924 cm<sup>-1</sup>. After deprotonation with NaOH to form sodium carboxylate (-COO-Na), the asymmetric stretching and symmetric stretching vibrations of the carbonyl (C=O) in BT and PT shift to 1548, 1555 cm<sup>-1</sup>, and 1370, 1382 cm<sup>-1</sup>, respectively. Additionally, the two O-H bending vibration peaks of the carboxylic acid group around 1310 and 924 cm<sup>-1</sup> disappear. These changes indicate that the -COOH group has been converted to the sodium carboxylate group (-COONa) after alkalization with NaOH.

We compared the powder XRD patterns of the carboxylates BT, PT, and BP (Fig. 1c). The diffraction peaks of these three substances are clearly visible, indicating that they possess specific crystal structures. Field emission scanning electron microscopy (FE-SEM) characterization provides a visual representation of the particle morphology and size. As shown in Fig. S9 (ESI†), BT exhibits a regular bulk morphology with sizes ranging from 1 to 3 µm, while PT has a nanoscale particle size, which may be attributed to the better planarity of bithiophene compared to phenylthiophene, facilitating the ordered molecular stacking. The thermal stability of the materials was also investigated using thermogravimetric analysis (TGA), determining the thermal decomposition temperatures to be 548, 495, and 626 °C for BT, PT, and BP, respectively, based on a 5% weight loss (Fig. 1d). As far as we know, the thermal decomposition temperature of BT is among one of the highest  $T_d$  values reported for organic carboxylates to date (Table S2, ESI†). The excellent thermal stability is beneficial for maintaining the structure and performance during charge and discharge processes.

The solubility of electrode materials in the electrolyte has a significant impact on the cycling stability of sodium-ion batteries (SIBs). To evaluate the solubility of BT and PT in the electrolyte, we prepared electrode sheets of BT and PT and immersed them in the electrolyte solution (1.0 M NaCF<sub>3</sub>SO<sub>3</sub>, TETRAGLYME = 100 vol%). We then measured the UV-visible absorption spectra of the electrolyte at different time intervals (1, 3, 7, and 15 days). As shown in Fig. S11 (ESI<sup>†</sup>), the initial electrolyte was almost transparent, and the solution remained colorless and transparent even after soaking for 15 days. This indicates that both PT and BT have poor solubility in the electrolyte.

To further investigate the electrochemical performance of BT and PT, we assembled half cells using metallic sodium as the counter electrode and 1.0 M NaCF<sub>3</sub>SO<sub>3</sub> (TETRAGLYME = 100 vol%) as the electrolyte. The cyclic voltammetry (CV) curves of the anode were recorded at a scan rate of 0.2 mV s<sup>-1</sup>, with a potential window of 0.1-2.5 V. As shown in Fig. S15a (ESI†), BT exhibits a pair of redox peaks located at 0.95/0.61 V, ascribed to the insertion/extraction of sodium ions in the C=O functional group, indicating a one-step electron transfer process during the redox reaction. The redox peaks of PT were located at 0.91/ 0.61 V (Fig. S16a, ESI†). Notably, the nearly overlapping CV curves in subsequent cycles indicate that the electrode materials show good reversibility.

The cycling performance of BT, PT, and BP was then investigated (with the cells activated at a current density of 0.2C before cycling), as shown in Fig. 2 and Fig. S12, S13 (ESI†). The initial capacities of the BT, PT, and BP electrodes at a current density of 0.2C were 201, 200, and 208 mA h  $g^{-1}$ , respectively. To eliminate the capacity contribution from conductive carbon black (Super P), we tested Super P separately at 0.2C, finding its capacity to be approximately 20 mA h  $g^{-1}$ indicating a very low contribution to the electrode materials' capacity. After removing the capacity of the conductive carbon black, the initial capacities of the three materials were close to their theoretical capacities (with theoretical capacities of BT, PT, and BP being 180, 183, and 187 mA h  $g^{-1}$ , respectively). Therefore, it can be concluded that the capacity of the cells primarily originates from the electrode materials. After 400 cycles at a current density of 0.2C, BT, PT, and BP exhibited capacity retention rates of 99.1%, 92.5%, and 88.3%, respectively (Fig. 2a and Fig. S10a, S11a, ESI†). We also tested the long-term cycling performance of the electrodes at a current density of 2C. The batteries assembled with the three materials initially showed a high reversible capacity of 150 mA h g<sup>-1</sup>, with capacity retention rates of 90.1%, 85.3%, and 81.8% for BT, PT, and BP. After 1500 cycles (Fig. 2c and Fig. S10b, S11b, ESI†). Additionally, the BT electrode not only exhibited good cycling stability but also demonstrated excellent rate performance. As shown in Fig. 2b, when the current density increased from 0.2C to 2C, the reversible discharge capacity decreased from 198 mA h g<sup>-1</sup> to 146 mA h g<sup>-1</sup>. When the current density was reduced back to 0.2C, the reversible discharge capacity recovered to 190 mA h g<sup>-1</sup>, close to the initial value. Throughout the entire process, the coulombic efficiency remained nearly at 100%. This indicates that the battery experiences minimal energy loss during the charging and discharging

ChemComm Communication

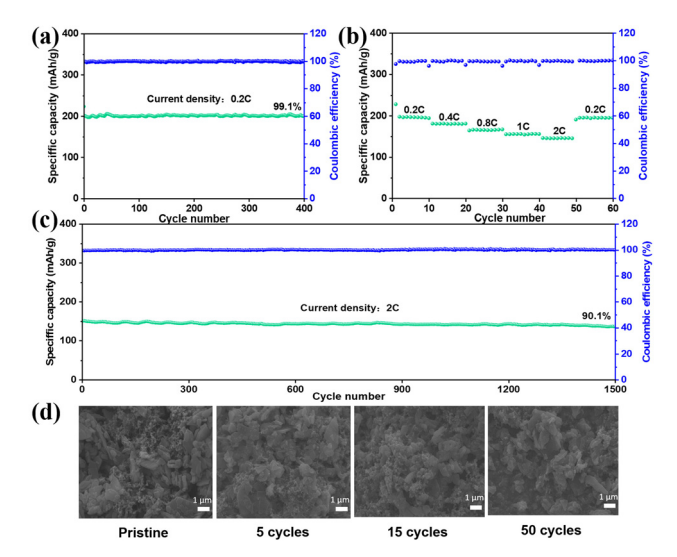


Fig. 2 (a) Cycle performance and coulomb efficiency of the BT electrode at 0.2C current density; (b) the rate performance of BT at different current densities (0.2C-2.0C); (c) long-term cycle performance of BT at 2.0C current density; and (d) SEM images of the BT electrode during different cycles.

process, reflecting its good performance and high energy conversion efficiency. We also examined the SEM images of the BT electrode at different cycles (original, 5th, 15th, and 50th cycles) (Fig. 2d). It can be observed that the physical contact between BT and Super P remained very tight and stable during cycling, showing no significant differences with increasing cycle numbers. These results indicate that the BT electrode is stable during the sodium insertion/extraction process.

The electrochemical impedance spectroscopy (EIS) measurements were also performed to study the diffusion of sodium ions in the electrolyte, the charge transfer through the solid electrolyte interphase (SEI), and their diffusion within the electrodes. As shown in Fig. S15b and S16b (ESI†), the EIS data were fitted using an equivalent circuit (Fig. S17, ESI†), and the results are shown in Table S3 (ESI†). The initial charge transfer resistances ( $R_{ct}$ ) for the BT and PT electrodes were 199.5  $\Omega$  and 281.2  $\Omega$ , respectively, which decreased to 188.2  $\Omega$  and 269  $\Omega$  after the first cycle. This phenomenon can be attributed to the formation of the electrode/ electrolyte interface (SEI), leading to reduced ohmic resistance and accelerated electron transfer rates. After 50 cycles, the resistance of BT stays almost the same while that of PT decreases to 262.7  $\Omega$ . Interestingly, BT demonstrated smaller  $R_{\rm ct}$  and contact resistance  $(R_f)$  compared to PT, and the impedance of the BT electrode shows the least change after cycling. This might be attributed to BT's faster electron transport rate, ensuring its excellent cycling and rate performance. Furthermore, the low interfacial charge transfer resistance reflects the rapid kinetics of the redox reactions in the BT electrode. We measured the sodium ion diffusion coefficient  $(D_{Na}^{+})$  using the galvanostatic intermittent titration technique (GITT). As the discharge process progressed, the ion diffusion coefficient gradually decreased, and during the charging process, it slowly decreased and then suddenly increased. Consequently, the minimum  $D_{Na}^{+}$  was observed at the end of discharge (around 0.1 V). Finally, we calculated the average  $D_{Na}^{+}$  values based on the ion diffusion coefficient calculation equation, which were 4.29  $\times$  10<sup>-8</sup> cm<sup>2</sup> S<sup>-1</sup> and 3.07  $\times$ 10<sup>-8</sup> cm<sup>2</sup> S<sup>-1</sup> (Fig. S15d and S16d, ESI†), with BT exhibiting the highest ion diffusion coefficient. This indicates that the BT electrode has good diffusion kinetics, which also explains its excellent rate performance even at high current densities.

We further studied how the molecular structures of the electrode materials affect the electrochemical properties, with the assistance of DFT calculations. Tables S4-S6 (ESI†) show the energy levels and energy gaps of the highest occupied orbital (HOMO) and lowest unoccupied orbital (LUMO) of each molecule before and after sodium storage. It can be seen that the introduction of thiophene rings reduces the energy level of the LUMO and raises the HOMO energy level, as a result, BT exhibited a smaller band gap (4.21 eV) (Fig. 3a). Previous studies have suggested that a small energy gap  $(E_{gap})$  in electrode materials has the potential to obtain good battery performance. At the same time, we used molecular electrostatic potential (MESP) to predict the possible binding sites of BT, PT and BP with Na<sup>+</sup>. Nucleophilic reactions tend to occur in MESP regions with positive potentials (red regions), while electrophilic reactions occur in MESP regions with more negative potentials (blue regions). As shown in the figure, the blue region around carboxyl oxygen in BT has a lower potential, indicating that C=O in -COO-Na may be the binding site for sodium ions.<sup>31</sup> The energy required for the two-step sodium storage reaction of BT (BT-Na and BT-2Na) is -1.41 eV and -0.51 eV, respectively (Fig. 3b). This requires more energy than the two-step sodium storage reactions of PT (-1.35 eV and -0.47 eV) (Fig. S18, ESI†) and BP (-1.04 eV and-0.48 eV) (Fig. S19, ESI†), indicating that BT has a stable structure after the oxidation reaction for sodium storage.<sup>32</sup>

To gain deeper insights into the sodium storage mechanism, we investigated the BT electrode sheets disassembled at different cutoff voltages during the sodium insertion/extraction process using FT-IR and XPS tests. We selected five characteristic states during the discharge/charge process, labeled in Fig. 4b as (a) 2.00 V, (b) 0.50 V, (c) 0.10 V, (d) 0.65 and (e)

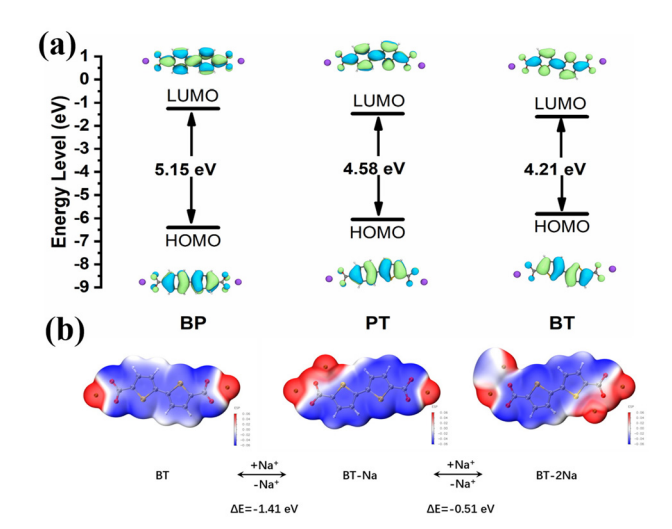
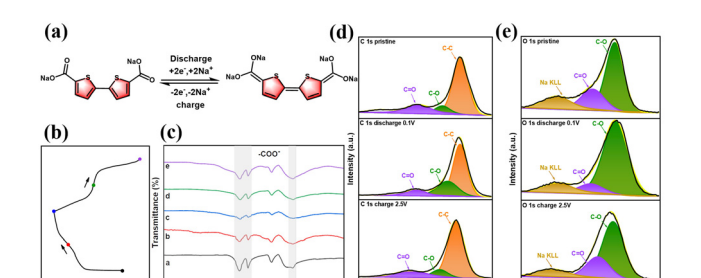


Fig. 3 (a) LUMO and HOMO energy and distribution calculated by BT, PT and BP; and (b) combination of the MESP distribution and potential energy  $\Delta E$  of BT with different Na<sup>+</sup> numbers.



Communication

Fig. 4 (a) Reaction mechanism of BT; (b) BT with marked points at different discharge and charge states; (c) FT-IR spectroscopy; (d) XPS C 1s spectrum; and (e) XPS O 1s spectrum.

2.50 V. As shown in Fig. 4c, the peaks around 1550 cm<sup>-1</sup> and 1370 cm<sup>-1</sup> correspond to the asymmetric and symmetric stretching vibrations of the C=O bonds in carboxylates, respectively. These peaks gradually decrease during discharge and increase during charging, indicating a typical transformation from carbonyl to enol. Therefore, these observations confirm that the C=O group serves as an active site during the charge and discharge processes. We further conducted XPS tests. In the C 1s spectrum (Fig. 4d), we clearly identified the C=O signal in the original electrode, with a binding energy of approximately 288 eV. When discharged to 0.1 V, the intensity of the C=O group weakened as the C-O group increased (around 286 eV), indicating that the C=O bond was reduced to a C-O bond, forming sodium enol. After charging, the intensity of the C=O bond peak increased as the intensity of the C-O bond peak decreased. This storage mechanism is further confirmed in the O 1s spectrum (Fig. 4e), which shows the reversible conversion from C=O (approximately 533 eV) to C-O bonds (approximately 531.8 eV). This further demonstrates the role of the C=O group as an active site during the charge and discharge processes. It shows that the reaction mechanism of BT may be as shown in Fig. 4a. During the discharge process, the BT molecule is occupied by two sodium ions, and the charging process is the reverse reaction of this process.

As discussed above, BT exhibits excellent electrochemical performance in half-cells, then, we further evaluated its performance in full batteries using commercial sodium vanadate (NVP) as the cathode material (Fig. S21a, ESI†). The redox mechanism and electrochemical performance of NVP are referenced in the literature,<sup>33</sup> with the charging/discharging voltage range for the NVP cathode being 2.5-3.6 V and that for the BT anode being 0.1-2.5 V. Based on the charging and discharging curves of the anode and cathode, we set the voltage range for the full battery to 1.5-3.5 V. At a current density of 100 mA g<sup>-1</sup>, the full battery demonstrated a reversible capacity of 82 mA h g<sup>-1</sup> (based on the weight of NVP) after 200 cycles, along with a high capacity retention rate of 88% (Fig. S21b, ESI†). The successful assembly of the BT and NVP full batteries indicates that BT is a promising organic anode material for sodium ion batteries.

In summary, we designed and synthesized two organic carboxylates, BT and PT, with bithiophene and phenylthiophene as the core structures, respectively. BT with bithiophene exhibits better planarity and enhanced  $\pi$ -conjugation, effectively addressing the common solubility issues and improving electronic conductivity. BT provides a reversible capacity of up to 201 mA h g<sup>-1</sup> and retains 99.1% of its capacity after 400 cycles at a current density of 0.2C. Even more impressively, at a current density of 2C, the BT electrode maintains a capacity retention rate of 90.1% after 1500 cycles.

Haoyu Yin: conceptualization, investigation, methodology, software, data curation, writing - original draft, visualization. Jingfu Chen: data curation, software, formal analysis. Junhong Tan: methodology, validation. Cheng Zhong: software, supervision. Fei Wu: conceptualization, formal analysis, writing review & editing, project administration. Linna Zhu: super vision, conceptualization, formal analysis, project administration, writing - review & editing, funding acquisition.

The authors are thankful for the support from Fundamental Research Funds for the Central Universities (SWU-XDJH202314).

## Data availability

Data will be available on request.

### Conflicts of interest

There are no conflicts to declare.

#### Notes and references

- 1 J. H. Huang and L. Shi, et al., Small Struct., 2023, 4, 9.
- 2 M. Mohammadiroudbari and J. H. Huang, et al., J. Mater. Chem. A, 2023, 11, 16901.
- 3 P. K. Nayak and L. T. Yang, et al., Angew. Chem., Int. Ed., 2018, 57, 102–120.
- 4 C. Delmas, Adv. Energy Mater., 2018, 8, 9.
- 5 J. Q. Deng and W. B. Luo, et al., Adv. Energy Mater., 2018, 8, 17.
- 6 Y. H. Liu and Y. H. Xu, et al., ACS Nano, 2013, 7, 3627-3634.
- 7 C. L. Wang and Y. Xu, et al., J. Am. Chem. Soc., 2015, 137, 3124-3130.
- 8 C. Ma and X. L. Zhao, et al., Angew. Chem., Int. Ed., 2018, 57, 8865-8870. 9 K. K. Jia and L. N. Zhu, et al., ChemSusChem, 2021, 14, 3124-3130.
- 10 B. Häupler and A. Wild, et al., Adv. Energy Mater., 2015, 5, 34.
- 11 K. K. Jia and J. W. Zhang, et al., J. Colloid Interface Sci., 2022, 623, 637-645. 12 Z. Q. Luo and L. J. Liu, et al., Angew. Chem., Int. Ed., 2018, 57, 9443–9446.
- 13 Y. S. Luo and K. K. Jia, et al., ChemSusChem, 2024, 17, e202301847.
- 14 J. W. Zhang and H. T. Liu, et al., J. Mater. Chem. A, 2023, 11, 2711–2717.
- 15 J. W. Zhang and J. F. Chen, et al., ACS Sustainable Chem. Eng., 2023, 11. 17849-17856.
- 16 J. F. Chen and H. Y. Yin, et al., Adv. Funct. Mater., 2024, 11, 2411362.
- 17 K. Q. Qin and K. Holguin, et al., Chem. Commun., 2021, 57, 2360-2363.
- 18 C. Luo and X. L. Fan, et al., Chem, 2017, 3, 1050-1062.
- 19 C. Luo and J. J. Shea, et al., J. Power Sources, 2020, 453, 5.
- 20 G. F. Zhao and Y. H. Zhang, et al., ACS Energy Lett., 2020, 5, 1022-1031.
- 21 S. Gu and S. F. Wu, et al., J. Am. Chem. Soc., 2019, 141, 9623-9628.
- 22 K. K. Jia, H. T. Liu and F. Wu, J. Mater. Chem. A, 2022, 10, 14917-14922.
- 23 C. Ma and L. Wu, et al., Chem. Mater., 2018, 30, 8426-8430.
- 24 C. Ma and L. Y. Wang, et al., J. Mater. Chem. A, 2021, 9, 11530-11536.
- 25 J. J. Shea and C. Luo, ACS Appl. Mater. Interfaces, 2020, 12, 5361–5380.
- 26 Y. C. Wu and Y. Chen, et al., Chem. Commun., 2019, 55, 10856-10859. 27 K. Q. Qin and J. H. Huang, et al., Energy Environ. Sci., 2020, 13,
- 3950-3992.
- 28 J. Huang and S. Li, et al., Small, 2024, 20(14), 2308113.
- 29 C. X. Peng and G. H. Ning, et al., Nat. Energy, 2017, 2, 9.
- 30 A. Choi and Y. K. Kim, et al., J. Mater. Chem. A, 2014, 2, 14986-14993.
- 31 L. M. Cui and L. M. Zhou, et al., Nano Energy, 2019, 65, 8.
- 32 P. Y. Han and F. S. Liu, et al., Angew. Chem., Int. Ed., 2021, 60, 23596-23601.
- 33 G. F. Li and J. X. Wang, et al., Energy Storage Mater., 2022, 47, 1-12.